Resonant states in the Schrödinger equation solved using the Green's function method*

Wentao Zeng (曾文涛)[1,2] Zehao Lin (林泽昊)[3,2] Yiran Wang (王一然)[4,5,2] Shuangquan Zhang (张双全)[1]
Jinniu Hu (胡金牛)[6] Ying Zhang (张颖)[2†]

[1]State Key Laboratory of Nuclear Physics and Technology, School of Physics, Peking University, Beijing 100871, China
[2]Department of Physics, School of Science, Tianjin University, Tianjin 300354, China
[3]National Laboratory of Solid-State Microstructures, Collaborative Innovation Center of Advanced Microstructures, School of Physics, Nanjing University, Nanjing 210093, China
[4]Institute of High Energy Physics, Chinese Academy of Sciences, Beijing 100049, China
[5]School of Physical Sciences, University of Chinese Academy of Sciences, Beijing 100049, China
[6]School of Physics, Nankai University, Tianjin 300071, China

Abstract: The Schrödinger equation with Woods-Saxon type potentials is solved using the Green's function (GF) method. Taking nucleus ^{40}Ca as an example, we show that the GF results for both bound and resonant single-neutron states are consistent with those obtained using the shooting and scattering matrix methods, respectively. Explicitly, three different recipes (GFI, GFII, and GFIII) are used to determine the energies and widths of resonant states. The GFI method directly extracts the resonant energy and width from the calculated density of states after removing the contributions of free particles. The GFII method identifies the resonant states by examining the flip of the density of states, whereas the GFIII method searches for the resonant states as poles of the modulus of GF on the complex energy plane. We find that the GFI method is effective for resonant states with narrow widths. For resonant states with broad widths, the GFII and GFIII methods are more accurate and effective. We also verify that the energies, widths, and density distributions of resonant states obtained using the GF method exhibit a rather weak dependence on the box size.

Keywords: Schrödinger equation, resonant states, Green's function method

DOI: 10.1088/1674-1137/ae118a **CSTR:** 32044.14.ChinesePhysicsC.50024103

I. INTRODUCTION

Resonant states are commonly observed in atomic, nuclear, and particle physics. Among all types of resonances, one-particle shape resonance is the simplest case that results in potential scattering of a particle by an unexcited target or simply in a potential field with a confining potential barrier [1]. In nuclear physics, since Tanihata et al. discovered the neutron halo in ^{11}Li in 1985 [2], scholars observed that the continuum spectrum, particularly the low-lying resonant states with a small angular momentum l therein, plays an important role in nuclei far from the β-stability line [3−5]. In addition, the single-particle resonances provide the main contribution to many collective excitations such as giant resonances [6, 7].

Many theoretical methods have been developed to study the single-particle resonant states in a given potential. Some of these methods are based on traditional scattering techniques, such as the R-matrix method [8, 9], scattering matrix (SM) method [7, 10−13], K-matrix method [14], Jost function method [15−17], and scattering phase shift method [18−20]. Moreover, some methods originally used for studying bound states have been extended to study single-particle resonant states, including the complex scaling method (CSM) [21−25], analytic continuation in the coupling constant (ACCC) method [26−30], real stabilization method (RSM) [31, 32], complex momentum representation (CMR) method [33−37], and complex-scaled Green's function (CGF) method [38−40].

Green's function (GF) [41−46], a useful mathematical tool, can provide another option for solving single-particle resonant states. It can simultaneously provide the information for both bound and continuum states, de-

Received 30 July 2025; Accepted 10 October 2025; Accepted manuscript online 11 October 2025

* This work was partly supported by the National Key R&D Program of China 2024YFE0109803, the National Natural Science Foundation of China (12435006, 12475149), the Natural Science Foundation of Guangdong Province (2024A1515010911), the National Key Laboratory of Neutron Science and Technology (NST202401016), and the High-performance Computing Platform of Peking University

† E-mail: yzhangjcnp@tju.edu.cn

pending on the boundary conditions. In the non-relativistic mean-field model, GF was initially used in the Hartree-Fock-Bogoliubov (HFB) theory to treat the continuum quasiparticle states in the presence of pairing [42, 47]. Subsequently, GF was used to calculate densities required in the self-consistent density functionals [48−50], where the quasiparticle resonances can be identified from the occupation and pair number densities [48, 51]. In the relativistic counterpart, the relativistic mean-field theory formulated using GF was first introduced in 2014 and successfully applied to study single-neutron resonant states [52]. The study was extended to single-proton and single-hyperon resonant states, respectively [53, 54]. The relativistic continuum Hartree-Bogoliubov (RCHB) theory was combined with the GF method to investigate the quasiparticle resonances and halo phenomena near the drip line [55, 56]. Note that in these studies, the resonance energy and width were obtained from the peak of density of states (DOS) calculated using GF subtracting the contribution from the free scattering states (denoted as GFI). Subsequently, two additional recipes were proposed to determine the resonant energies and widths of broad resonances with higher precision. Refs. [57, 58] proposed to scan the DOS in the fourth quadrant of the complex energy plane and identify the resonance states as the flip of the DOS when crossing the poles of GF (denoted as GFII), whereas Refs. [59, 60] proposed to search the resonant states directly as the poles of GF in the fourth quadrant of the complex energy plane (denoted as GFIII).

The above three recipes GFI, GFII and GFIII have been developed to determine the resonant states in the Dirac equation. In this paper, we check the feasibility of these recipes to identify the single-neutron resonances in the Schrödinger equation. By taking the Woods-Saxon type mean-field and spin-orbit potentials in ^{40}Ca as an example, we calculate the DOS using the GF method for both bound and continuum states. Subsequently, the single-neutron resonant energies and widths are determined using the GFI, GFII, and GFIII methods respectively, and we compare their results in detail. The remainder of this paper is organized as follows: Sec. II presents the theoretical framework to solve the Schrödinger equation using the GF method. Sec. III discusses the DOSs for the bound and resonant states obtained using the GF method and compares in detail the energies and widths of the resonant states obtained using the three recipes. Finally, a summary is presented in Sec. IV.

II. THEORETICAL FRAMEWORK

The stationary Schrödinger equation is

$$H\phi = \epsilon\phi, \tag{1}$$

where H is the single-particle Hamiltonian, ϕ is the single-particle wave function, and ϵ is the corresponding energy. The Hamiltonian can be expressed as

$$H = -\frac{\hbar^2}{2\mu}\nabla^2 + V(\boldsymbol{r}), \tag{2}$$

with μ representing the mass of the neutron and $V(\boldsymbol{r})$ the single-particle potential. Here $V(\boldsymbol{r})$ includes the Woods-Saxon mean-field potential $V_q(r)$ and spin-orbit potential $V_{ls}(r)$ with the spherical symmetry:

$$V(\boldsymbol{r}) = V_q(r) + V_{ls}(r), \tag{3}$$

in which

$$V_q(r) = \frac{V_0}{1+\mathrm{e}^{(r-R)/a}}, \tag{4}$$

and

$$V_{ls} = \frac{1}{2\mu c^2}\frac{1}{r}\frac{\mathrm{d}V_q}{\mathrm{d}r}\boldsymbol{l}\cdot\boldsymbol{s}. \tag{5}$$

The single-particle GF for the Schrödinger equation (1) is defined as

$$[\epsilon - H]\mathcal{G}(\boldsymbol{r}\sigma, \boldsymbol{r}'\sigma', \epsilon) = \delta(\boldsymbol{r}-\boldsymbol{r}')\delta_{\sigma\sigma'}, \tag{6}$$

with $\boldsymbol{r}$ representing the space coordinate and σ the spin of the particle. This GF can be expressed by a complete set of eigenstates $\phi_n(\boldsymbol{r}\sigma)$ and the corresponding eigenvalues ϵ_n of the Hamiltonian H, *i.e.*,

$$\mathcal{G}(\boldsymbol{r}\sigma, \boldsymbol{r}'\sigma', \epsilon) = \sum_n \frac{\phi_n(\boldsymbol{r}\sigma)\phi_n^*(\boldsymbol{r}'\sigma')}{\epsilon - \epsilon_n}. \tag{7}$$

Obviously, the eigenstates of the Schrödinger equation are the poles of the GF. In the DOS [61]

$$n(\epsilon) = \sum_n \delta(\epsilon - \epsilon_n), \tag{8}$$

the bound states will appear as δ peaks at real ϵ_n. The resonant states locate in the fourth quadrant of the complex energy plane with the energies $\epsilon_n = \varepsilon_R - \mathrm{i}\Gamma/2$, where ε_R and Γ are the resonance energy and width, respectively [57, 62]. We can demonstrate that the DOS can be calculated using the integral of the GF in the coordinate $\boldsymbol{r}$ space as

$$n(\epsilon) = -\frac{1}{\pi}\sum_{\sigma}\int \mathrm{d}\boldsymbol{r}\,\mathrm{Im}[\mathcal{G}(\boldsymbol{r}\sigma,\boldsymbol{r}\sigma,\epsilon)]. \tag{9}$$

In a spherical system, the DOS can be expressed as a superposition of the partial wave DOSs:

$$n(\epsilon) = \sum_{lj} n_{lj}(\epsilon), \tag{10}$$

with l and j being the angular momenta of the partial wave. On the other hand, the GF can also be expanded as

$$\mathcal{G}(\boldsymbol{r}\sigma,\boldsymbol{r}'\sigma',\epsilon) = \sum_{ljm} \mathrm{Y}_{ljm}(\hat{\boldsymbol{r}}\sigma)\frac{\mathcal{G}_{lj}(r,r',\epsilon)}{rr'}\mathrm{Y}^{*}_{ljm}(\hat{\boldsymbol{r}}'\sigma'), \tag{11}$$

where $\mathrm{Y}_{ljm}(\hat{\boldsymbol{r}}\sigma)$ is the spin spherical harmonic, and $\mathcal{G}_{lj}$ represents the radial GF with the angular momenta l and j. Therefore, for a partial wave state with fixed quantum numbers l and j, the DOS is given by

$$n_{lj}(\epsilon) = -\frac{2j+1}{\pi}\int \mathrm{d}r\,\mathrm{Im}\left[\mathcal{G}_{lj}(r,r,\epsilon)\right]. \tag{12}$$

The radial GF $\mathcal{G}_{lj}(r,r',\epsilon)$ can be calculated as

$$\begin{aligned}\mathcal{G}_{lj}(r,r',\epsilon) = \frac{1}{w(\epsilon)}\big\{&\theta(r-r')u^{(1)}_{lj}(r')u^{(2)}_{lj}(r)\\ &+\theta(r'-r)u^{(1)}_{lj}(r)u^{(2)}_{lj}(r')\big\},\end{aligned} \tag{13}$$

where $\theta(r-r')$ is the step function, and $w(\epsilon)$ is the r-independent Wronskian function defined by

$$w(\epsilon) \equiv \frac{\hbar^2}{2\mu}\left[u^{(1)}_{lj}(r)\frac{\mathrm{d}u^{(2)}_{lj}(r)}{\mathrm{d}r} - u^{(2)}_{lj}(r)\frac{\mathrm{d}u^{(1)}_{lj}(r)}{\mathrm{d}r}\right]. \tag{14}$$

Wave functions $u^{(1)}_{lj}(r)$ and $u^{(2)}_{lj}(r)$ satisfy the radial Schrödinger equation,

$$u''(r,\epsilon) + \left[\frac{2\mu\epsilon}{\hbar^2} - \frac{l(l+1)}{r^2} - \frac{2\mu}{\hbar^2}V(r)\right]u(r,\epsilon) = 0, \tag{15}$$

and are obtained from the asymptotic behaviors at $r\to 0$ and $r\to\infty$, respectively. At $r\to 0$, the radial wave function $u^{(1)}_{lj}(r)$ is regular and can be expanded into powers of r as in the SM approach [13]. At $r\to\infty$, the radial wave function $u^{(2)}_{lj}(r)$ satisfies

$$u^{(2)}_{lj}(r) = krh^{(1)}_{l}(kr), \tag{16}$$

where $k^2 = \frac{2\mu\epsilon}{\hbar^2}$, and $h^{(1)}_{l}(kr)$ is the spherical Hankel function of the first kind. Note that, for the bound states with the real negative energy ϵ, the spherical Hankel function of the first kind $h^{(1)}_{l}(kr)$ with imaginary argument kr can be reduced to an exponential decaying function of the coordinate r in the asymptotic region. For the continuum states with a positive real part of energy, $h^{(1)}_{l}(kr)$ can be reduced to an oscillating function of r in the asymptotic region. Therefore, the outside boundary condition in Eq. (16) naturally considers the different asymptotic behaviors for bound and continuum states according to their energies. Consequently, both the bound and continuum states can be included in the GF (13) using the same form of boundary conditions.

III. RESULTS AND DISCUSSION

In the following, we take the single-neutron potential of ^{40}Ca as an example to examine the bound and resonant states in the Schrödinger equation obtained using the GF method. The corresponding parameters of the Woods-Saxon potential (3) are taken as $V_0 = -57.0$ MeV, $a = 0.67$ fm, $R = 4.06945$ fm, and $\hbar^2/2\mu = 20.22671$ MeV$\cdot$fm^2. To identify the resonant states, we follow three different methods using the GF obtained in Sec. I. To check the stability of the results of the resonant states, we select the coordinate space as $R_{\rm box} = 10, 20, 30$ fm with a mesh size $\mathrm{d}r = 0.1$ fm.

A. GFI Method

In the first method, GFI [52], the partial wave DOS $n_{lj}(\epsilon)$ (12) can be calculated using the integral of GF in the coordinate space with a complex energy $\epsilon = \varepsilon + \mathrm{i}\kappa$, where ε and κ are both real numbers representing the real and imaginary parts of the energy, respectively. In this method, the imaginary part of energy κ has a fixed small positive value 1×10^{-3} MeV to visualize the δ peak for the bound state (if any). We can plot the DOS $n_{lj}(\epsilon)$ as a function of the real part of energy ε to search the bound or resonant states. The energy step to plot $n_{lj}(\epsilon)$ is taken as $\mathrm{d}\varepsilon = 1\times10^{-3}$ MeV. With both the given mean-field and spin-orbit potentials in Eq. (3), the calculated DOSs $n_{lj}(\epsilon)$ are shown in Fig. 1 for different partial waves obtained with the box size $R_{\rm box} = 20$ fm.

In the energy region $\varepsilon < 0$, the bound state (if any) will appear as a sharp peak with an artificial width 2κ. As shown in Fig. 1, we can extract the bound state energies at the peaks in $s_{1/2}, p_{1/2}, p_{3/2}, d_{3/2}, d_{5/2}, f_{5/2}$, and $f_{7/2}$ partial waves. These energies are listed in Table 1, in comparison with the results obtained using the shooting method with the box boundary condition in the same coordinate space. As shown, the single-neutron energies of bound states obtained from the two methods correspond within a precision of 10^{-3} MeV, which is determined by the energy step $\mathrm{d}\varepsilon$.

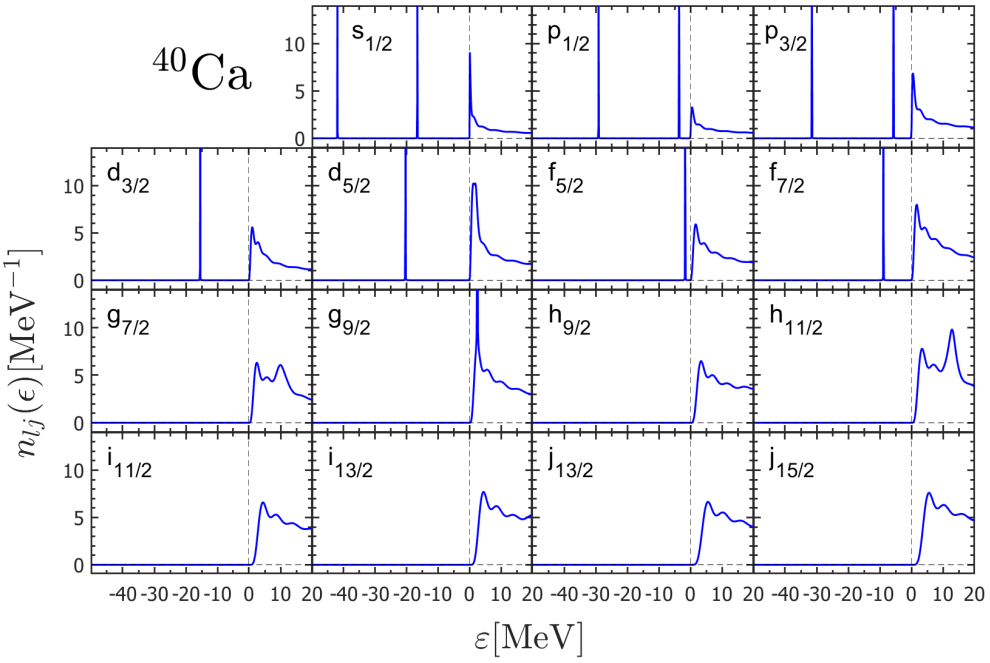

Fig. 1. (color online) Neutron DOSs $n_{lj}(\epsilon)$ ($\epsilon=\varepsilon+\mathrm{i}\kappa$ with $\kappa=1\times10^{-3}$ MeV) for different partial waves in ^{40}Ca calculated using the GF method, with Woods-Saxon type mean-field and spin-orbit potentials shown in the box $R_{\max}=20$ fm (solid line). The dashed vertical line at $\varepsilon=0$ marks the continuum threshold.

Table 1. Single-neutron energies (in MeV) of bound states in ^{40}Ca obtained using the GFI and shooting methods. Box size $R_{\rm box}=20$ fm and mesh size d$r=0.10$ fm are adopted.

nlj	GFI	Shooting
$1s_{1/2}$	−41.961	−41.9607
$2s_{1/2}$	−16.587	−16.5870
$1p_{1/2}$	−29.077	−29.0770
$2p_{1/2}$	−3.557	−3.5572
$1p_{3/2}$	−31.508	−31.5080
$2p_{3/2}$	−5.648	−5.6479
$1d_{3/2}$	−15.466	−15.4658
$1d_{5/2}$	−20.349	−20.3493
$1f_{5/2}$	−1.630	−1.6298
$1f_{7/2}$	−8.838	−8.8379

Just above the continuum threshold $\varepsilon=0$, the DOS exhibits sharp upward inclines with some peaks or oscillations above. According to Ref. [52], this is primarily contributed by the free particle scattering states. To remove their contributions, we can subtract the DOS $n^0_{lj}(\epsilon)$ calculated using only the centrifugal barrier but no mean-field potentials ($V_q(r)=0$) from the total DOS $n_{lj}(\epsilon)$ and obtain the residual DOS $n^r_{lj}(\epsilon)=n_{lj}(\epsilon)-n^0_{lj}(\epsilon)$ that is contributed only from the resonant states (if any). From the residual DOS, we can identify the resonant states and obtain the corresponding energy and width information.

The neutron DOSs $n_{lj}(\epsilon)$,$n^0_{lj}(\epsilon)$, and $n^r_{lj}(\epsilon)$ above the continuum threshold for different partial waves in ^{40}Ca calculated by GF are shown in Fig. 2. From the residual DOSs $n^r_{lj}(\epsilon)$, we observe some apparent peaks in $d_{5/2}$, $g_{7/2}$, $g_{9/2}$, $h_{11/2}$ and $i_{13/2}$ partial waves, which clearly correspond to the resonant states. We can take the peak energy as the resonant energy and the full width at half maximum (FWHM) to calculate the resonant width Γ:

$$\mathrm{FWHM}=2\left(\kappa+\frac{\Gamma}{2}\right). \tag{17}$$

Among these partial waves, $g_{9/2}$ has a typical sharp resonant state at the energy $\varepsilon_R=2.478$ MeV with a considerably small width of $\Gamma=0.023$ MeV. Since the energy step is taken as d$\varepsilon=1\times10^{-3}$ MeV, the extracted energy and width are also truncated to the third decimal place (10^{-3} MeV). In contrast, the residual DOS $n^r_{lj}(\epsilon)$ in the $d_{3/2}$ partial wave has some small peaks within a wide energy region 2 ~ 8 MeV. The energy and width of resonant state here are difficult to identify. Taking $g_{9/2}$ and $d_{3/2}$ as two distinct examples, their DOSs $n^r_{lj}(\epsilon)$ are magnified and compared in Fig. 3. To check the dependence of the DOSs on the box sizes, we also show the results calculated with box sizes $R_{\rm box}=10$ and 30 fm. For the narrow resonance in the $g_{9/2}$ partial wave in Fig. 3 (a), the peak structures calculated using different $R_{\rm box}$ values are almost the same. Thus, the resonant energy and width obtained from the peaks calculated using different box sizes

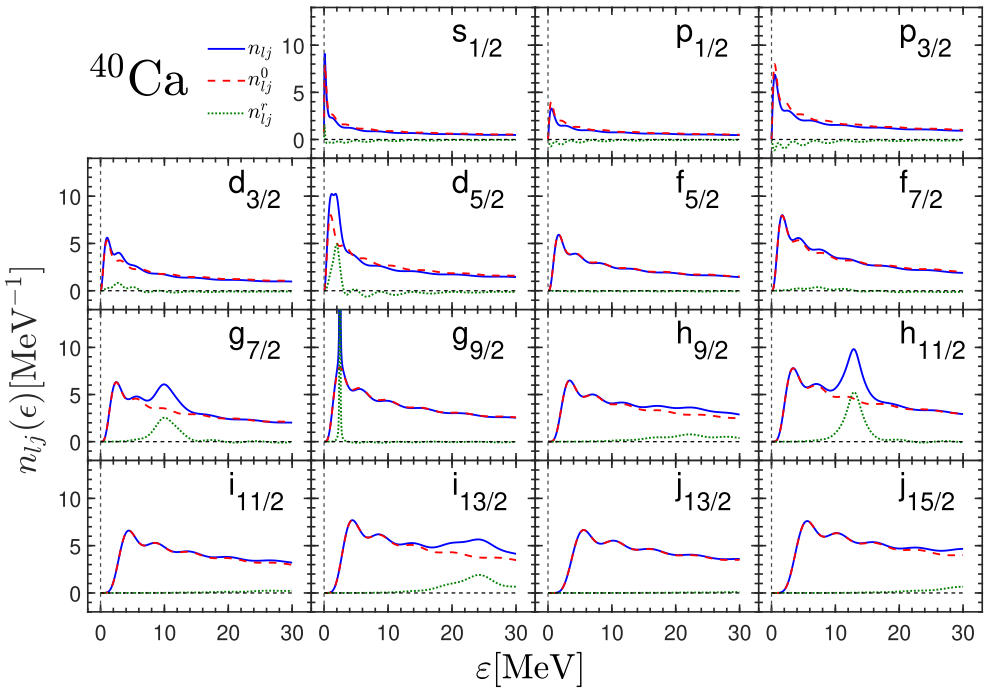

Fig. 2. (color online) Neutron DOSs $n_{lj}(\epsilon)$ ($\epsilon=\varepsilon+\mathrm{i}\kappa$ with $\kappa=1\times10^{-3}$ MeV) for different angular momentum partial waves in ^{40}Ca calculated using the GF method with Woods-Saxon type mean-field and its spin-orbit potentials (solid line), with only centrifugal barrier $n^0_{lj}(\epsilon)$ (dashed line) and their differences $n^r_{lj}(\epsilon)=n_{lj}(\epsilon)-n^0_{lj}(\epsilon)$ (dotted line) in the box $R_{\rm box}=20$ fm. The dashed vertical line at $\varepsilon=0$ marks the continuum threshold.

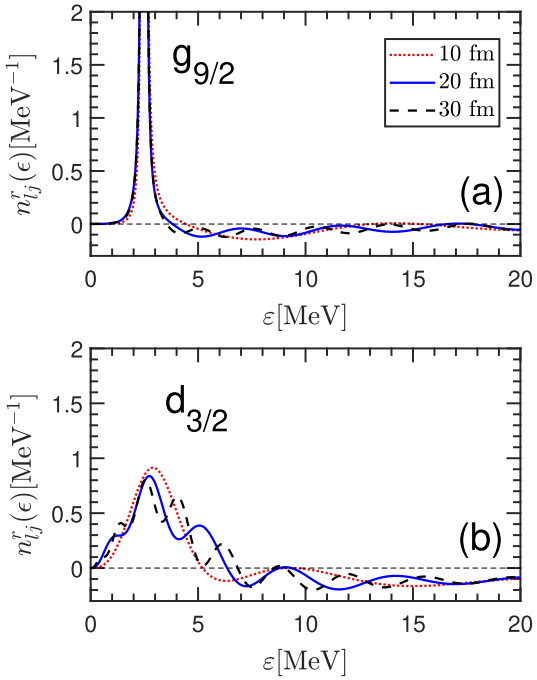

Fig. 3. (color online) The residual DOSs $n^r_{lj}(\epsilon)$ ($\epsilon=\varepsilon+\mathrm{i}\kappa$ with $\kappa=1\times10^{-3}$ MeV) calculated with different box sizes $R_{\rm box}=10,20,30$ fm are shown for (a) $g_{9/2}$ and (b) $d_{3/2}$ partial waves. The same mesh size $\mathrm{d}r=0.1$ fm is adopted.

are identical, as shown in Table 2 (GFI). In contrast, for the broad resonance in the $d_{3/2}$ partial wave in Fig. 3 (b), the DOS $n^r_{lj}(\epsilon)$ changes significantly with different box sizes. We can still take the center energy of the highest peak as the resonant energy and the corresponding FWHM for the resonant width. The results thus obtained are also listed in Table 2 (GFI). We easily observe that the obtained energy and width for the broad $d_{3/2}$ resonance sensitively depend on the adopted box size.

As shown in Fig. 2, except for the narrow resonant state in the $g_{9/2}$ partial wave, other partial waves $d_{3/2}, d_{5/2}$, $g_{7/2}, h_{11/2}$, and $i_{13/2}$ have peaks in the residual DOSs $n^r_{lj}(\epsilon)$ with large widths. We list their resonant energies and widths determined using GFI with different box sizes in Table 2 (GFI). Their resonant energies and widths are mostly all dependent on the box size. Therefore, the GFI method is reliable for determining the resonant energies and widths for the narrow resonant states, but obtaining this information with high accuracy is difficult for the broad resonant states.

B. GFII Method

Resonant states manifest as poles situated within the fourth quadrant of the single-particle complex energy plane. Consequently, the DOS exhibits a δ peak at the pole position. The DOS in the complex energy plane $n_{lj}(\epsilon)$, where $\epsilon=\varepsilon_r+\mathrm{i}\varepsilon_i$ can be calculated using the GF with scanning the real and imaginary parts of energies ε_r and ε_i in the fourth quadrant. It can be demonstrated that [58], near the energy of resonant states $\epsilon_R=\varepsilon_R-\mathrm{i}\Gamma/2$,

Table 2. Resonant energies ε_R and widths Γ of single-neutron resonant states nlj in ^{40}Ca obtained using three different methods (GFI, GFII, GFIII) and the SM with box sizes $R_{\rm box} = 10, 20, 30$ fm and the same mesh size 0.10 fm. All in MeV.

nl_j		10 fm		20 fm		30 fm	
		ε_R	Γ	ε_R	Γ	ε_R	Γ
$2d_{3/2}$	GFI	2.902	2.356	2.732	1.674	2.556	3.196
	GFII	2.7143	4.8350	2.7133	4.8498	2.7133	4.8496
	GFIII	2.7143	4.8350	2.7133	4.8496	2.7133	4.8496
	SM	2.7140	4.8362	2.7133	4.8500	2.7133	4.8500
$2d_{5/2}$	GFI	1.860	1.096	1.946	1.325	2.018	1.401
	GFII	1.7610	1.3296	1.7603	1.3310	1.7603	1.3312
	GFIII	1.7610	1.3296	1.7603	1.3310	1.7603	1.3310
	SM	1.7610	1.3298	1.7603	1.3312	1.7603	1.3312
$1g_{7/2}$	GFI	10.040	3.643	10.025	4.016	10.582	3.546
	GFII	10.2206	3.5296	10.2208	3.5278	10.2207	3.5276
	GFIII	10.2206	3.5296	10.2208	3.5276	10.2208	3.5276
	SM	10.2206	3.5294	10.2208	3.5276	10.2208	3.5276
$1g_{9/2}$	GFI	2.478	0.023	2.478	0.022	2.478	0.022
	GFII	2.4780	0.0240	2.4780	0.0238	2.4780	0.0238
	GFIII	2.4780	0.0238	2.4781	0.0238	2.4781	0.0238
	SM	2.4780	0.0238	2.4780	0.0238	2.4780	0.0238
$1h_{11/2}$	GFI	12.799	2.678	12.940	2.899	12.880	2.312
	GFII	12.8877	2.6938	12.8880	2.6924	12.8880	2.6924
	GFIII	12.8877	2.6938	12.8880	2.6924	12.8880	2.6924
	SM	12.8878	2.6936	12.8880	2.6924	12.8880	2.6924
$1i_{13/2}$	GFI	24.685	8.662	24.250	7.610	23.211	8.661
	GFII	23.8506	9.4758	23.8470	9.4806	23.8469	9.4804
	GFIII	23.8489	9.4764	23.8470	9.4804	23.8470	9.4804
	SM	23.8502	9.4754	23.8470	9.4804	23.8470	9.4804

$$
\begin{aligned}
n_{lj}(\epsilon) &= \delta(\epsilon-\epsilon_R) \\
&= \begin{cases} -\dfrac{2j+1}{\pi}\int \mathrm{d}r\,\mathrm{Im}\left[\mathcal{G}_{lj}(r,r,\epsilon)\right], \\ \qquad \text{if } \varepsilon_i > -\Gamma/2, \\ \dfrac{2j+1}{\pi}\int \mathrm{d}r\,\mathrm{Im}\left[\mathcal{G}_{lj}(r,r,\epsilon)\right], \\ \qquad \text{if } \varepsilon_i < -\Gamma/2. \end{cases}
\end{aligned} \tag{18}
$$

In other words, when the imaginary part ε_i crosses before and after $-\Gamma/2$ at the resonant state, the value of DOS $n_{lj}(\epsilon)$ will change the sign. When the real part of the energy, ε_r, approaches the resonance energy ε_R, two distinct positive and negative peak structures emerge symmetrically before and after the imaginary part of the energy ε_i scanning across the value $-\Gamma/2$, serving as a signature of resonant states. To obtain the resonance energy and width with high accuracy, we must first determine the range for the energy scan. In principle, the bisection method can be employed to progressively narrow the ε_r scanning range based on the two peak structures discussed above. In practice, the rough resonant state information given by the GFI method can be used as a reference for the ε_r and ε_i scanning.

Taking partial waves $g_{9/2}$ and $d_{3/2}$ as examples, Fig. 4 shows the scanned DOS $n_{lj}(\epsilon)$ as a function of the real part energy ε_r with different imaginary part energies ε_i. As clearly shown in Fig. 4 (a), with different ε_i values, the peaks of $n_{lj}(\epsilon)$ in the $g_{9/2}$ partial wave all appear at the same real part energy $\varepsilon_r = 2.4780$ MeV with different heights. This center energy of the peaks corresponds to the resonant energy $\varepsilon_R = 2.4780$ MeV. Furthermore, with ε_i increasing from -0.0120 MeV to $\varepsilon_i = -0.0119$ MeV, the DOS inverses its negative values to positive values. We select the value $\varepsilon_i = -0.0119$ MeV that provides the largest absolute value $n_{lj}(\epsilon)$ to calculate the resonant width as $\Gamma = -2\varepsilon_i = 0.0238$ MeV. For partial wave $d_{3/2}$ in Fig. 4 (b), the peaks of DOS appear not to be symmetric

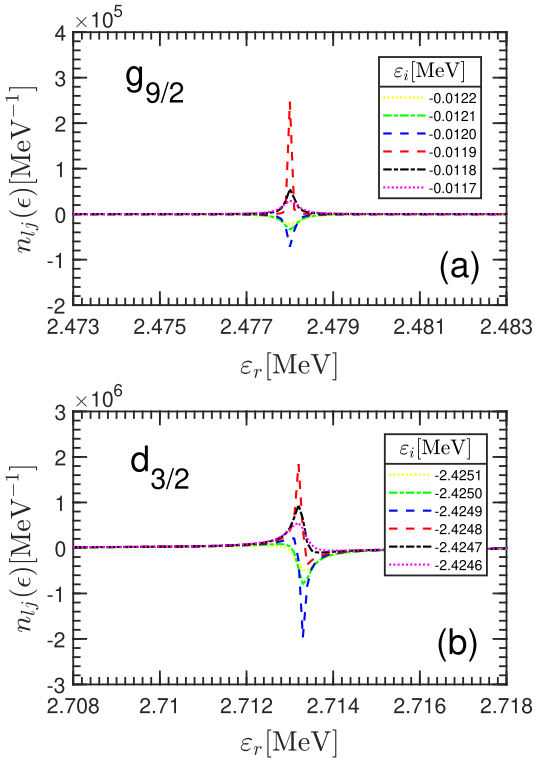

Fig. 4. (color online) Neutron DOSs $n_{lj}(\epsilon)$ calculated with different real and imaginary parts of energy ε_r and ε_i in the coordinate space with $R_{\rm box} = 20$ fm for (a) $g_{9/2}$ and (b) $d_{3/2}$ partial waves.

as those in partial wave $g_{9/2}$. As ε_i increases from -2.4249 MeV to $\varepsilon_i = -2.4248$ MeV, the DOS flips from the valley structure to the peak structure. Similarly, we take the DOS that provides the largest absolute value $n_{lj}(\epsilon)$ ($\varepsilon_i = -2.4249$ MeV) to identify the resonant energy and width, that is, $\varepsilon_R = \varepsilon_r = 2.7133$ MeV and $\Gamma = -2\varepsilon_i = 4.8498$ MeV. In this calculation, the step for the energy scanning is taken as 10^{-4} MeV, which determines our precision in identifying the resonant energies and widths.

Following the same procedures, we can obtain the resonant energies and widths for all the other partial waves. In Table 2, the resonant energies and widths determined using the GFII method with different box sizes are listed for comparison. Compared with those obtained using GFI, the results are less sensitive to the adopted box size. In particular, the GFII method with the box sizes $R_{\rm box} = 20$ fm and 30 fm provides consistent results within an accuracy of 10^{-4} MeV for both narrow and broad resonances.

C. GFIII Method

Inspired by the idea of the GFII method that the resonant states are identified by searching the extremes of DOSs, a more straightforward method was proposed in Refs. [59, 60] by probing the poles or extremes of the GF. To be more intuitive, we can integrate the modulus of GF $\mathcal{G}_{lj}(r,r,\epsilon)$ over coordinate r

$$G_{lj}(\epsilon) = \int {\rm d}r \left|\mathcal{G}_{lj}(r,r,\epsilon)\right|, \tag{19}$$

and search its extremes by scanning the real and imaginary parts (ε_r, ε_i) in the fourth quadrant of the complex energy plane. The resonant states will manifest themselves as peak structures at the resonant energy $\varepsilon_R = \varepsilon_r$ with a width $\Gamma = 2\varepsilon_i$.

Taking partial waves $g_{9/2}$ and $d_{3/2}$ as examples, Fig. 5 shows the three-dimensional plot of the integral $G_{lj}(\epsilon)$ as a function of the real and imaginary parts of energies ε_r and ε_i calculated with a box size of $R_{\rm box} = 20$ fm. In both panels, the peak structure representing the pole is apparent for the narrow resonance in $g_{9/2}$ and the broad resonance in $d_{3/2}$. From the peak structures, we can easily identify the resonant energies and widths at the center of the peak, which are $\varepsilon_R = \varepsilon_r = 2.4780$ MeV and $\Gamma = -2\varepsilon_i = 0.0238$ MeV for the $g_{9/2}$ partial wave and $\varepsilon_R = \varepsilon_r = 2.7133$ MeV and $\Gamma = -2\varepsilon_i = 4.8496$ MeV for the $d_{3/2}$ partial wave.

The GFIII method has been applied for all the partial waves calculated with different box sizes, and the obtained resonant energies and widths are also listed in Table 2. As the results show, the GFIII method is as effective as the GFII method, and both methods are less sensit-

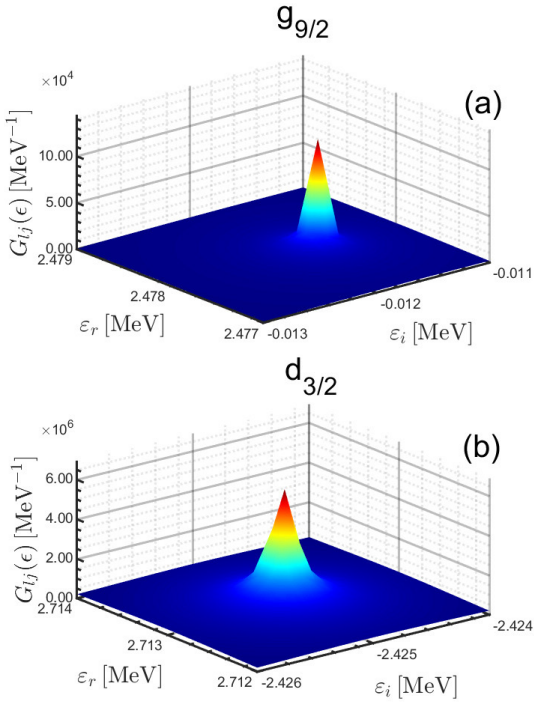

Fig. 5. (color online) Three-dimensional modulus $G_{lj}(\epsilon)$ calculated with different real and imaginary parts of energy ε_r and ε_i, in the coordinate space with $R_{\rm box} = 20$ fm for (a) $g_{9/2}$ and (b) $d_{3/2}$ partial waves.

ive to the adopted box size than the GFI method.

D. Discussion

In Table 2, we have listed the single-neutron resonant energies ε_R and widths Γ for different partial waves in ^{40}Ca obtained using the three methods GFI, GFII, and GFIII. To check the dependence on the box sizes, we perform the calculations using different box sizes $R_{\rm box} = 10$, 20, and 30 fm and the same mesh size $\mathrm{d}r = 0.1$ fm. For comparison, the corresponding results obtained using the SM method [13] are also included.

For the resonant state in partial wave $g_{9/2}$ with a small width, the GFI, GFII, and GFIII methods provide almost the same results as the SM, which are also not very dependent on the box sizes. For other partial waves that have relatively broad resonances, with the same box size, the results given by GFI are not very consistent with other methods. However, the results given by GFII and GFIII for these broad resonances are consistent with those obtained using the SM. Furthermore, the results of GFII, GFIII, and the SM are not sensitive to the box sizes for these broad resonances.

To further check the results' dependence on the box sizes, we can plot the partial wave density distribution at the resonant energy ε_R:

$$\rho_{lj}(r,\varepsilon_R) = -\frac{(2j+1)}{4\pi r^2}\frac{1}{\pi}\mathrm{Im}\left[\mathcal{G}_{lj}(r,r,\varepsilon_R)\right]. \tag{20}$$

Taking the narrow and broad resonances in partial waves $g_{9/2}$ and $d_{3/2}$ as examples, Fig. 6 shows their density distributions at the corresponding resonant energies ε_R calculated with box sizes $R_{\rm box} = 10, 20, 30$ fm. As shown in Table 2, the resonant energies obtained using GFI, GFII, and GFIII are the same $\varepsilon_R = 2.478$ MeV for the $1g_{9/2}$ resonant state. For $2d_{3/2}$, the resonant energy obtained using GFI is different from those of GFII and GFIII. The resonant energies obtained using GFII and GFIII are consistent, *i.e.*, $\varepsilon_R = 2.7143$ MeV with $R_{\rm box} = 10$ fm, and $\varepsilon_R = 2.7133$ MeV with $R_{\rm box} = 20, 30$ fm. We use these two resonant energies to plot the density distributions for $2d_{3/2}$ obtained with different box sizes correspondingly. From Fig. 6 (a), we observe that the density distribution of narrow resonant state in the $g_{9/2}$ partial wave behaves as a bound state. Its density distribution decreases quickly to be zero after $r \approx 8$ fm. In contrast, the broad resonance state in the $d_{3/2}$ partial wave in Fig. 6 (b) has obvious oscillating density distributions. However, for both narrow and broad resonances, the density distributions calculated using the GF method at their resonant energies are not sensitive to the box size. In particular, for the broad resonant state in the $d_{3/2}$ partial wave with the rapid oscillations in the density distribution, even with the small box size $R_{\rm box} = 10$ fm, it can still provide consistent density distributions with those obtained by the larger

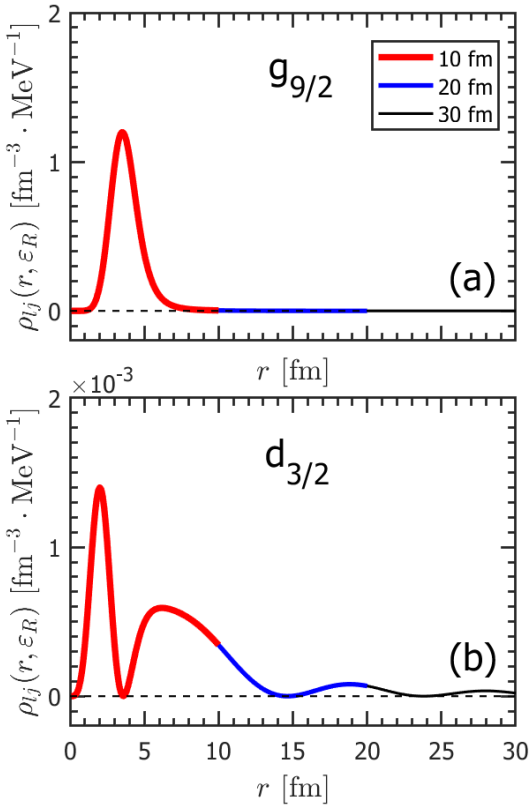

Fig. 6. (color online) Density distributions $\rho_{lj}(r,\varepsilon_R)$ at the resonant energies ε_R for single-neutron resonant state (a) $1g_{9/2}$ and (b) $2d_{3/2}$ calculated in the coordinate space with box sizes $R_{\rm box} = 10, 20, 30$ fm and the same mesh size $\mathrm{d}r = 0.1$ fm.

boxes up to $r = 10$ fm. The larger box sizes only display the density distribution in further region. This is attributed to the proper description of the wave functions for the continuum states given by the GF method. This can also explain why the resonant energies and widths are not sensitive to the box sizes given by the GFII and GFIII methods. We expect that the density distributions calculated using GF can properly include the contributions from the continuum states in the density functional theory.

Comparing the GFI, GFII, and GFIII methods to provide the resonant energies and widths, the GFI method reading from the DOSs calculated using a fixed small imaginary part energy is only reliable for the narrow resonant states. In contrast, the GFII and GFIII methods, which scan the poles of the DOSs and the GF with different real and imaginary part of energies, are reliable for both the narrow and broad resonant states. In practice, we can use GFI in the first step to locate the resonant states roughly and then use GFII or GFIII to scan the poles around this location with a higher precision.

IV. SUMMARY

In this paper, the Schrödinger equation with Woods-

Saxon type potentials for neutrons in ^{40}Ca is solved using the GF method. The bound and resonant states are obtained with the GF constructed using the wave functions with proper boundary conditions corresponding to their energies. The GF results for both bound and resonant single-neutron states are consistent with those obtained by the shooting and SM methods. Explicitly, three different recipes (GFI, GFII, and GFIII) are used to determine the energies and widths of resonant states. With the GFI method, by subtracting the contributions of free particle from the total DOS, we can identify the resonant states and obtain the corresponding energy and width information. In the GFII method, the resonant states are identified using the flip of DOS as the imaginary part of energy changes. More straightforwardly, in the GFIII method, the resonant states are identified as poles of the modulus of GF scanned in the fourth quadrant of the complex energy plane. Compared with the results given by the SM, we find that GFI is only reliable for the narrow resonant states, whereas GFII and GFIII are effective for both the narrow and broad ones. Additionally, we observe that the energies, widths, and density distributions of resonant states obtained using the GF method exhibit a rather weak dependence on the box size. We expect that the GF can provide the proper density distributions with the contributions from the continuum states in the density functional theory.

References

[1] V. I. Kukulin, V. Krasnopolsky, and J. Horácek, *Theory of resonances: Principles and Applications*, Vol. 3 (Springer Science & Business Media, 2013)
[2] I. Tanihata, H. Hamagaki, O. Hashimoto *et al.*, Phys. Rev. Lett. **55**, 2676 (1985)
[3] J. Dobaczewski, W. Nazarewicz, T. R. Werner *et al.*, Phys. Rev. C **53**, 2809 (1996)
[4] M. Yamagami, Phys. Rev. C **72**, 064308 (2005)
[5] A. Volya and V. Zelevinsky, Phys. At. Nucl. **77**, 969 (2014)
[6] P. Curutchet, T. Vertse, and R. J. Liotta, Phys. Rev. C **39**, 1020 (1989)
[7] L.-G. Cao and Z.-Y. Ma, Phys. Rev. C **66**, 024311 (2002)
[8] E. P. Wigner and L. Eisenbud, Phys. Rev. **72**, 29 (1947)
[9] P. Descouvemont and D. Baye, Rep. Prog. Phys. **73**, 036301 (2010)
[10] K. T. R. Davies and M. Baranger, Ann. Phys. (N. Y.) **19**, 383 (1962)
[11] T. Vertse, K. Pál, and Z. Baloch, Comput. Phys. Commun. **27**, 309 (1982)
[12] L. Ferreira, E. Maglione, and R. Liotta, Phys. Rev. Lett. **78**, 1640 (1997)
[13] Á. Baran, C. Noszály, and T. Vertse, Comput. Phys. Commun. **228**, 185 (2018)
[14] J. Humblet, Phys. Rev. C **42**, 1582 (1990)
[15] S. Rakityansky, S. Sofianos, and K. Amos, Il Nuovo Cimento B (1971-1996) **111**, 363 (1996)
[16] B.-N. Lu, E.-G. Zhao, and S.-G. Zhou, Phys. Rev. Lett. **109**, 072501 (2012)
[17] B.-N. Lu, E.-G. Zhao, and S.-G. Zhou, Phys. Rev. C **88**, 024323 (2013)
[18] J. R. Taylor, *Scattering Theory: The Quantum Theory of Nonrelativistic Collisions* (John Wiley & Sons, New York, 1972)
[19] P. Kennedy, N. Dombey, and R. L. Hall, Int. J. Mod. Phys. A **19**, 3557 (2004)
[20] Z.-P. Li, J. Meng, Y. Zhang *et al.*, Phys. Rev. C **81**, 034311 (2010)
[21] B. Simon, Int. J. Quantum Chem. **14**, 529 (1978)
[22] B. Gyarmati and A. T. Kruppa, Phys. Rev. C **34**, 95 (1986)
[23] N. Moiseyev, Phys. Rep. **302**, 212 (1998)
[24] J.-Y. Guo, X.-Z. Fang, P. Jiao *et al.*, Phys. Rev. C **82**, 034318 (2010)
[25] M. Shi, Q. Liu, Z.-M. Niu *et al.*, Phys. Rev. C **90**, 034319 (2014)
[26] N. Tanaka, Y. Suzuki, K. Varga *et al.*, Phys. Rev. C **59**, 1391 (1999)
[27] S.-C. Yang, J. Meng, and S.-G. Zhou, Chin. Phys. Lett. **18**, 196 (2001)
[28] S.-S. Zhang, J. Meng, and J.-Y. Guo, Chin. Phys. C **27**, 1095 (2003)
[29] X.-D. Xu, S.-S. Zhang, A. J. Signoracci *et al.*, Phys. Rev. C **92**, 024324 (2015)
[30] R. Takatsu, Y. Suzuki, W. Horiuchi *et al.*, Phys. Rev. C **107**, 024314 (2023)
[31] L. Zhang, S.-G. Zhou, J. Meng *et al.*, Phys. Rev. C **77**, 014312 (2008)
[32] H. Mei, H. Chen, and J.-M. Yao, Chin. Phys. C **33**, 101 (2009)
[33] G. Hagen and J. S. Vaagen, Phys. Rev. C **73**, 034321 (2006)
[34] N. Li, M. Shi, J.-Y. Guo *et al.*, Phys. Rev. Lett. **117**, 062502 (2016)
[35] Y.-J. Tian, T.-H. Heng, Z.-M. Niu *et al.*, Chin. Phys. C **41**, 044104 (2017)
[36] X.-W. Wang and J.-Y. Guo, Phys. Rev. C **104**, 044315 (2021)
[37] H.-T. Zhang, C.-F. Chen, X.-R. Zhou *et al.*, Chin. Phys. C **49**, 044101 (2025)
[38] X.-X. Shi, M. Shi, Z.-M. Niu *et al.*, Phys. Rev. C **94**, 024302 (2016)
[39] M. Shi, X.-X. Shi, Z.-M. Niu *et al.*, Eur. Phys. J. A **53**, 40 (2017)
[40] X.-X. Shi, Q. Liu, M. Shi *et al.*, Chin. Phys. C **42**, 114105 (2018)
[41] G. Bertsch and S. Tsai, Phys. Rep. **18**, 125 (1975)
[42] S. Belyaev, A. Smirnov, S. Tolokonnikov *et al.*, Yad. Fiz **45**, 1263 (1987)
[43] E. Tamura, Phys. Rev. B **45**, 3271 (1992)
[44] S. Shlomo, Nucl. Phys. A **539**, 17 (1992)
[45] D. L. Foulis, Phys. Rev. A **70**, 022706 (2004)
[46] T. Nakatsukasa and K. Yabana, Phys. Rev. C **71**, 024301 (2005)
[47] M. Matsuo, Nucl. Phys. A **696**, 371 (2001)
[48] S. Fayans, S. Tolokonnikov, and D. Zawischa, Phys. Lett. B **491**, 245 (2000)
[49] H. Oba and M. Matsuo, Phys. Rev. C **80**, 024301 (2009)
[50] Y. Zhang, M. Matsuo, and J. Meng, Phys. Rev. C **83**,

054301 (2011)
[51] Y. Zhang and X.-Y. Qu, Phys. Rev. C **102**, 054312 (2020)
[52] T.-T. Sun, S.-Q. Zhang, Y. Zhang *et al*., Phys. Rev. C **90**, 054321 (2014)
[53] T.-T. Sun, Z.-M. Niu, and S.-Q. Zhang, J. Phys. G: Nucl. Part. Phys. **43**, 045107 (2016)
[54] S.-H. Ren, T.-T. Sun, and W. Zhang, Phys. Rev. C **95**, 054318 (2017)
[55] T.-T. Sun, Sci. Sin.-Phys. Mech. Astron. (in Chinese) **46**, 012006 (2016)
[56] X.-Y. Qu, H. Tong, and S.-Q. Zhang, Phys. Rev. C **105**, 014326 (2022)
[57] C. Chen, Z.-P. Li, Y.-X. Li *et al*., Chin. Phys. C **44**, 084105 (2020)
[58] T.-T. Sun, L. Qian, C. Chen *et al*., Phys. Rev. C **101**, 014321 (2020)
[59] Y.-T. Wang and T.-T. Sun, Nucl. Sci. Tech. **32**, 46 (2021)
[60] T.-T. Sun, Z.-P. Li, and P. Ring, Phys. Lett. B **847**, 138320 (2023)
[61] E. N. Economou, *Green's functions in quantum physics* (Springer, 2006)
[62] T. Berggren, Nucl. Phys. A **109**, 265 (1968)